JOURNAL OF AIRCRAFT
Vol. 42, No. 5, September–October 2005

Automatic Transition Prediction and Application to High-Lift Multi-Element Configurations

Andreas Krumbein*
DLR, German Aerospace Center, D-38108 Brunswick, Germany

A Reynolds-averaged Navier–Stokes (RANS) solver, a laminar boundary-layer code, and an e^N-database method for transition prediction were coupled in order to perform RANS computations of two-dimensional high-lift multi-element systems with automatic laminar-turbulent transition prediction and transitional flow regions. It will be shown that the coupled system represents a RANS-based computational-fluid-dynamics tool that provides accurate values of the transition locations during the ongoing RANS computation automatically and fast without the need for the intervention by the code user. Thus, RANS computations of two-dimensional high-lift multi-element configurations with transition can be carried out without a priori knowledge of the transition characteristics of the specific flow problem. The coupling structure and the underlying algorithm of the transition prediction procedure as well as the physical modeling of transitional flow regions and their generation in the RANS computational grid are described. The testing of the transition prediction procedure is described and documented. The computational results are compared to experimental data.

Nomenclature

C_P = constant that acts as turbulence production limiter of a transport equation turbulence model
C^T = underrelaxation factor
c_d = drag coefficient
c_f = skin-friction coefficient
c_l = lift coefficient
c_p = pressure coefficient
D_t = turbulence destruction term of a transport equation turbulence model
F = reduced frequency
FLG_{lt} = laminar-turbulent flag for the code internal eddy viscosity μ_t^{code}
f = frequency
H_i = incompressible shape parameter, $H_i = \delta_i^* / \Theta_i$
k = turbulent kinetic energy
k_{cyc} = number of RANS cycles for the transition location iteration that represents the interval between two calls of the transition prediction module
l_{tr} = transition length
N_e = maximum number of the geometry elements
$N|_{x^T}$ = limiting N factor at the transition location x^T
n_e = number of the current geometry element
n_{elem} = number of transition points at an element of the configuration
P = point of the computational grid
P_F = field point of the computational grid
P_S = surface point of the computational grid
P_t = turbulence production term of a transport equation turbulence model
Re_l = Reynolds number based on the length l, that is, $U_e l / \nu_e$
s = arc length starting at the stagnation point
Tu_∞ = freestream turbulence intensity
t = time
U = tangential flow velocity
U_e = tangential flow velocity at the boundary-layer edge
$\boldsymbol{v}$ = mean flow velocity vector
$\boldsymbol{v}'$ = perturbation of the velocity vector
x = longitudinal coordinate of the configuration in the global coordinate system of the RANS solver or tangential direction of the local coordinate system originating in a surface point
x_0 = x coordinate of the point where a perturbation enters the unstable zone
x^T = longitudinal coordinate value of the transition point
$\tilde{x}^T$ = longitudinal coordinate value of the transition point, underrelaxed
y = vertical coordinate of the configuration in the global coordinate system of the RANS solver or wall normal direction of the local coordinate system originating in a surface point
α_i = local spatial amplification rate
γ = intermittency function, $\gamma(\sigma) = 1 - \exp(-0.412\xi^2)$
δ = boundary-layer thickness, $\delta(\sigma)$
δ^* = displacement thickness,

$$\delta^*(\sigma) = \int_0^{\delta(\sigma)} \left[1 - \frac{(\rho U)(y)}{\rho_e U_e}\right] \mathrm{d}y$$

δ_i^* = incompressible displacement thickness,

$$\delta_i^*(\sigma) = \int_0^{\delta(\sigma)} \left[1 - \frac{U(y)}{U_e}\right] \mathrm{d}y$$

ε = lower limit for convergence criterion
Θ_i = incompressible momentum loss thickness,

$$\Theta_i(\sigma) = \int_0^{\delta(\sigma)} \frac{U(y)}{U_e}\left[1 - \frac{U(y)}{U_e}\right] \mathrm{d}y$$

λ = constant of the intermittency function
μ_e = dynamic viscosity at the boundary-layer edge
μ_t = eddy viscosity
ν_e = kinematic viscosity at the boundary-layer edge
ξ = variable of the intermittency function, $(\sigma - \sigma_{\mathrm{tr}}^{\mathrm{beg}})/\lambda$
ρ = density
ρ_e = density at the boundary-layer edge
σ = length coordinate along the streamline of the boundary-layer edge
ω = specific turbulent dissipation rate
ω = circular frequency

Received 23 April 2004; presented as Paper 2004-2543 at the AIAA 34th Fluid Dynamics Conference and Exhibit, Portland, OR, 28 June–1 July 2004; revision received 11 August 2004; accepted for publication 12 August 2004. Copyright © 2004 by Andreas Krumbein. Published by the American Institute of Aeronautics and Astronautics, Inc., with permission. Copies of this paper may be made for personal or internal use, on condition that the copier pay the $10.00 per-copy fee to the Copyright Clearance Center, Inc., 222 Rosewood Drive, Danvers, MA 01923; include the code 0021-8669/05 $10.00 in correspondence with the CCC.

*Research Scientist, Design Engineer, Institute of Aerodynamics and Flow Technology, Numerical Methods, Lilienthalplatz 7; andreas.krumbein@dlr.de. Member AIAA.

Subscripts

beg = beginning of the transitional flow region
code = inside the code
comp = computational, computed
cyc = RANS cycle
e = element or edge of the boundary layer
elem = element, as slat, main, or flap
end = end of the transitional flow region
exp = experimental
F = field
fixed = fixed in the computation
ft = fully turbulent
hi = high
i = counter of the surface points; incompressible
init = initial
j = counter of the transition points
l = counter of the transition iteration steps
lo = low
low = lower side
max = maximum
nose = nose of the airfoil
nst = nearest
nu = nonunique
old = old
q = placemarker for upper side or lower side
S = surface
sep = at the separation point
stag = at the stagnation point
T = transition
t = turbulent
tr = at transition onset, transitional region, with transition
trail = trailing edge
upp = upper side

I. Introduction

THE modeling of laminar-turbulent transition in Reynolds-averaged Navier–Stokes (RANS) solvers is a necessary requirement for the computation of flows over airfoils and wings in the aerospace industry because it is not possible to obtain quantitatively correct results if the laminar-turbulent transition is not taken into account. For the design process of wings in industry, there exists the demand for a RANS-based computational-fluid-dynamics (CFD) tool that is able to handle flows automatically and autonomously with laminar-turbulent transition.

The first steps towards the setup of such a tool were made, for example, in Ref. 1, where a RANS solver and an e^N method[2,3] based on linear stability theory and the parallel flow assumption were applied, and in Ref. 4, where a RANS solver, a laminar boundary-layer method,[5] and an e^N method were coupled. There, the boundary-layer method was used to produce highly accurate laminar, viscous layer data to be analyzed by a linear stability code. Hence, the very expensive grid adaptation necessary to produce accurate viscous layer data directly from the Navier–Stokes grid was avoided. The use of an e^N-database method[6] results in a coupled program system that is able to handle automatically transition prediction. Alternative approaches using a transition closure model or a transition/turbulence model directly incorporated into the RANS solver are documented in Refs. 7–9.

At the DLR, German Aerospace Center the block-structured RANS code FLOWer[10] is used together with the laminar boundary-layer method in Ref. 5 and the e^N-database method in Ref. 6. The laminar boundary-layer method and the e^N-database method form a so-called transition prediction module that is coupled to the RANS solver and that interacts with the RANS solver during the computation.[11,12] Presently, the transition prediction module of FLOWer can be applied to two-dimensional one-element or multi-element configurations.

The description of transitional flow regions in FLOWer is done either by the application of point transition or by the application of physical models of transitional flow. The application of point transition means that turbulence quantities, which are suppressed in the laminar part of the flow, suddenly become active at the location of transition onset. This procedure results in a sudden change of the flow quantities in this area. Because of the effects of numerical dissipation, an artificial transition region is generated in a computation without physical transition modeling. However, the sudden change of the flow quantities is often strong enough to prevent the convergence of the iterative transition prediction process.[13] In addition, the application of point transition generates a strong upstream influence so that the artificial transition region starts considerably upstream of the transition location. In two-dimensional airfoil flows, an upstream influence up to 10% of the chord length of the airfoil can be observed. The physical modeling of transitional flow overcomes this problem and leads to a more stable coupled computational procedure of RANS code and transition prediction module on the one hand and to better results of the numerical simulation on the other.

In Ref. 14 it was described how the FLOWer code was extended to handle multi-element configurations with transition. The extensions were performed in two steps. First, a generalized infrastructure in the FLOWer code with respect to the transition prediction module was built up and tested, that is, the code was changed in such a way that the transition prediction module can be activated now for arbitrary multi-element configurations independent of the block topology and the grid structure. Second, the transition prediction module was coupled to the generalized infrastructure. In the framework of Ref. 14, the first extension step was documented. Thus, Ref. 14 has the character of a progress report. In the present paper, the second extension step is described and finalizes the documentation of the treatment of automatically predicted transition locations and their application in a RANS code with physically modeled transitional flow regions for two-dimensional multi-element configurations. At the time that Ref. 14 was written, the transition prediction module was not yet coupled to the extended FLOWer code; the locations of laminar separation determined by the FLOWer code were supposed to represent the laminar-turbulent transition locations in a first step. In many cases, this assumption leads to a good approximation of the real transition point, particularly for low-Reynolds-number airfoil flows, when transition does not occur before the laminar boundary layer separates. Now the transition locations are determined by the e^N-database method of Ref. 6.

The main objective of the work presented in this paper is to supply a reliable infrastructure in a RANS code and a coupling structure between the RANS code and the transition prediction module so that both program systems can be used for the computation of two-dimensional multi-element high-lift systems of aircraft including transitional flow regions and automatically predicted transition locations. In the end, it will be shown that the coupled system consisting of the FLOWer code and the transition prediction module represents a RANS-based CFD tool that provides accurate values of the transition locations during the ongoing RANS computation automatically and fast without the need for the intervention of the user.

A method and an algorithm for the coupling of the transition prediction module and thereby for detecting the laminar-turbulent transition locations based on linear stability theory were implemented in the FLOWer code. For each element of a high-lift configuration on the upper and lower side, the laminar separation point will be detected, and the transition fixed there during the transient phase of the RANS computation. When the computation has reached a stable state and the lift coefficient has reached a certain convergence level, the transition point will be detected by the transition prediction module, and the transition will be fixed there as long as a new laminar separation point or a new transition point is detected. The intermittency function and three transition length models were implemented and validated in a variety of test computations for two selected high-lift multi-element test cases. This paper focuses on the structure of the transition prediction module and its coupling to the FLOWer code, the underlying algorithm of the transition prediction procedure,[4–6,11,12] and the testing of the algorithm. The testing is described and documented by a number of commented plots of the results of the transition prediction procedure and of the transition length models. The computed pressure and skin-friction distributions are presented, and the c_p distributions are compared to experimental data. Finally, the global lift and drag coefficients are compared with experimental findings.

II. Implementation

FLOWer is a three-dimensional, compressible RANS code for steady or unsteady flow problems and uses structured body-fitted multiblock meshes. The code is based on a finite volume method and a cell-vertex spatial discretization scheme and uses an explicit Runge–Kutta time-integration scheme with multigrid acceleration. The influence of turbulence is taken into account by eddy-viscosity turbulence models according to the Boussinesq approximation. The transition handling is independent of the block topology of the computational grid and of the grid structure (structured, unstructured or hybrid grid).[11]

A. Coupling of the RANS Solver and the Transition Prediction Module

The complete coupled program system that is used for transition prediction with the RANS solver FLOWer consists of the RANS solver itself,[10] a laminar boundary-layer method for swept, tapered wings,[5] and a transition prediction method, which is provided with all necessary data, for example, boundary-layer parameters, by the laminar boundary-layer method. Besides a number of empirical transition criteria, the most general transition prediction method that is available in the FLOWer transition prediction module is an e^N-database method.[6]

The RANS solver communicates the surface-pressure distribution of the configuration as input data to the laminar boundary-layer method, the laminar boundary-layer method computes all of the boundary-layer parameters that are needed for the transition prediction method, and the transition prediction method determines new transition locations that are given back to the RANS solver. This coupled structure results in an iterative procedure for the transition locations within the iteration of the RANS equations.

After a certain number of iteration cycles k_{cyc} of the RANS solver, the transition prediction module is called. With the call of the module, the solution process is interrupted. The module analyzes the laminar boundary layers of specified components of the configuration, for example, one element of a two-dimensional airfoil configuration. The determined transition locations, $x_j^T(\text{cycle} = k_{\text{cyc}})$ with $j = 1, \ldots, n_{\text{elem}}$, where n_{elem} is the number of transition points, are communicated back to the RANS solver, which performs transition prescription by applying an transition setting algorithm,[11,12] and continues the solution process of the RANS equations. In so doing, the determination of the transition locations becomes an iteration process itself. The structure of the approach is outlined graphically in Fig. 1. At every call of the module, the surface pressure, $c_p(\text{cycle} = k_{\text{cyc}})$, along an airfoil element computed by the RANS solver, is used as input to the boundary-layer calculation. The viscous data calculated by the boundary-layer method are subsequently analyzed by the e^N-database method. The application of a boundary-layer method for the computation of all viscous data necessary for the transition prediction method ensures the high accuracy of the viscous data required by the e^N methods for the analysis of laminar boundary layers. Thus, as shown in Ref. 4, the large number of grid points near the wall for a high resolution of boundary layers, the adaptation of the Navier–Stokes grid in the laminar and turbulent boundary-layer regions, and the generation of new adapted grids for the RANS solver after every step of the transition location iteration are avoided, and the computational time can be massively reduced. The algorithm for the transition prediction iteration works as follows:

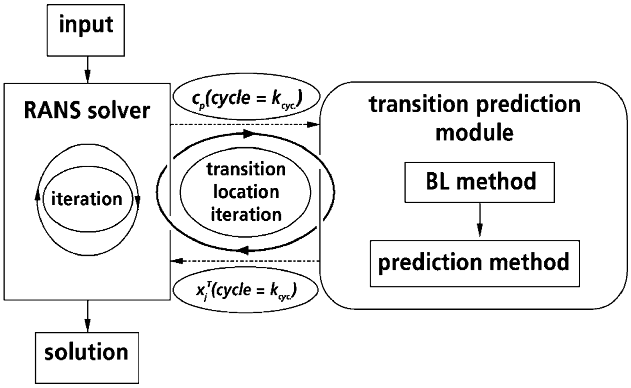

Fig. 1 Coupling structure of the RANS solver and the transition prediction module.

1) The RANS solver is started as if a computation with prescribed transition locations should be performed. In this moment, the transition locations are set far downstream on the upper and lower sides of the airfoil, for example, at the trailing edge. The RANS solver now computes a fully laminar flow over the airfoil.

2) During the solution process of the RANS equations, the laminar flow is checked for laminar separation points by the RANS solver. In the case that a laminar separation is detected, the separation point is used as an approximation of the transition location, the transition is fixed there, and the computation is continued.

3) The RANS equations are iterated until the lift coefficient $c_l = c_l(\text{cycles})$ has become constant with respect to the iteration cycles.

4) The transition prediction module is called. The laminar boundary-layer method determines the locations of laminar separation on upper and lower sides of the airfoil. The e^N-database method determines the transition locations on upper and lower sides of the airfoil. In the case that the e^N-database method does not detect a transition location as a result of Tollmien–Schlichting instabilities upstream of the current laminar separation point from the boundary-layer method, the laminar separation point is used as an approximation of the real transition point, and transition is fixed there.

5) The current coordinate $x_j^T(\text{cycle} = k_{\text{cyc}})$, which is used as a transition location, is underrelaxed. That is, as new transition locations the coordinates $\tilde{x}_j^T(\text{cycle} = k_{\text{cyc}})$, which are located downstream of the coordinates $x_j^T(\text{cycle} = k_{\text{cyc}})$, are used:

$$\tilde{x}_j^T(k_{\text{cyc}}) = C_j^T(k_{\text{cyc}}) x_j^T(k_{\text{cyc}}) \qquad \text{with} \qquad j = 1, \ldots, n_{\text{elem}} \tag{1}$$

with $C_j^T(k_{\text{cyc}}) > 1$. Only after the last step of the transition location iteration, $C_j^T(k_{\text{cyc}}) = 1$ is applied. This underrelaxation of the transition locations prevents the case that at an unconverged stage during the transition location iteration, transition coordinates are determined too far upstream, and might not be shifted downstream again.

6) As a convergence criterion, $\Delta\tilde{x}_j^{T,l} < \varepsilon$ with $\Delta\tilde{x}_j^{T,l} = |\tilde{x}_j^T(k_{\text{cyc}}^l) - \tilde{x}_j^T(k_{\text{cyc}}^{l-1})|$ is applied, where l is the current iteration step. In the case that the criterion is satisfied, the iteration for x_j^T is finished, else the algorithm loops back to station 2).

This transition location iteration procedure was very succesfully applied to single-element airfoil flows involving regions with adverse as well as favorable pressure gradients and cases with slow as well as quick growth of the Tollmien–Schlichting waves in Refs. 11–13, 15–18. In Ref. 12 it was shown that the final values of the converged transition locations are independent of the values of the initial transition locations. The same independence can be read for multi-element airfoils in Ref. 15.

B. e^N-Database Method

The e^N method used[5] applies

$$N|_{x^T} = -\int_{x_0}^{x^T} \alpha_i \, \mathrm{d}x \tag{2}$$

as a transition criterion. The limiting N factor $N|_{x^T}$ at the transition location x^T must be determined experimentally and represents the total amplification of a Tollmien–Schlichting wave in the boundary layer according to linear stability theory. The perturbation of the mean flow $\boldsymbol{v}$ of frequency f—$\boldsymbol{v}$ is assumed to be steady and well parallel—is described by a harmonic Tollmien–Schlichting wave

$$\boldsymbol{v}' = \boldsymbol{v}'_0(y)e^{i(\alpha x - \omega t)} \tag{3}$$

with the circular frequency $\omega = 2\pi f$ and $\alpha = \alpha_r + i\alpha_i$, where α_i can be expressed as a function of the shape parameter H_i; $Re_{\delta_i^*}$, the Reynolds number with respect to the incompressible displacement thickness δ_i^*; and the reduced frequency F,

$$\alpha_i = \alpha_i\left(H_i, Re_{\delta_i^*}, F\right) \tag{4}$$

Here

$$H_i = \delta_i^* \big/ \Theta_i \qquad \text{with} \qquad \delta_i^* = \int_0^\delta \left[1 - \frac{U(y)}{U_e}\right] \mathrm{d}y$$

$$\text{and} \qquad \Theta_i = \int_0^\delta \frac{U(y)}{U_e}\left[1 - \frac{U(y)}{U_e}\right] \mathrm{d}y \tag{5}$$

$$Re_{\delta_i^*} = \frac{U_e \rho_e \delta_i^*}{\mu_e} \tag{6}$$

and

$$F = \omega\mu_e \big/ \rho_e U_e^2 \tag{7}$$

As described in Refs. 5 and 19, the boundary layers of the similarity solution using the approach of Falkner and Skan were generated for 13 shape parameters H_i, which cover the range from highly accelerated up to separating flows. The growth of the boundary layer was simulated by varying $Re_{\delta_i^*}$. For each boundary layer, stability computations were completed for a sufficiently large range of excited frequencies. The results for the amplification rates α_i were stored in a database. The stability computation for a real boundary layer, using the database method, is executed for a given frequency f [Hz = 1/s] in the following way: at each grid point on the airfoil the properties f, $Re_{\delta_i^*}$, H_i, U_e, μ_e, and ρ_e are known. Evaluating F from the value of f, α_i is obtained from $\alpha_i = \alpha_i(H_i, Re_{\delta_i^*}, F)$ via interpolation in the database.

In Refs. 5 and 19, the use of the database is a high-quality approximation for the values resulting from a local linear stability code. In Refs. 4, 5, 16, and 19, it was shown that the Falkner–Skan approach approximates all relevant properties of the two-dimensional laminar boundary-layer flow around airfoils in practice, with high accuracy.

For the application of the e^N method, extensive experimental programs have been performed to determine the value of $N|_{x^T}$, which depends on the environmental disturbances in the flow. For free flight conditions $N|_{x^T} \approx 12$ was found for Tollmien–Schlichting waves. For wind tunnel-flows, which are normally characterized by relatively high disturbances, one often finds $N|_{x^T} \approx 6$. For wind-tunnel conditions Mack's relationship[20]

$$N|_{x^T} = -8.43 - 2.4\,\ln(Tu_\infty) \tag{8}$$

can be applied with some confidence.

C. Generation of Transitional Flow Regions

In the case that a new transition location has been determined, the laminar, transitional, and turbulent flow regions must be generated anew within the computational grid. The generation of the different regions is done by the setting of a real value flag FLG_{lt} at each point of the computational grid. FLG_{lt} is applied to the value of the turbulence production P_t of a transport equation turbulence model, which is computed for every point P in the flowfield. FLG_{lt} is applied in the following way:

$$P_t^{\text{code}}(P) = \min\left[P_t(P), D_t(P)C_P^{FLG_{\text{lt}}(P)}\right] \tag{9}$$

with $FLG_{\text{lt}}(P) = 0.0$ for a laminar grid point, $FLG_{\text{lt}}(P) = 1.0$ for a turbulent grid point, and $FLG_{\text{lt}}(P) = \gamma(P)$ for a transitional grid point, $\gamma(P)$ being the value of the intermittency function γ at the grid point P. D_t is the value of the turbulence destruction of a transport equation turbulence model, and C_P is a constant, which acts as a limiter on the turbulence production term for the source term of the turbulence model.[11,21] Thus, the source term of the turbulence model is controlled in such a way that its value is lower or equal zero in laminar regions. The default value for C_P in the FLOWer code is $C_P = 10$ for two-equation turbulence models of k-ω type and $C_P = 10^{10}$ for one-equation turbulence models.[21] The default value of C_P for one-equation turbulence models in effect turns off the production limitation in fully turbulent regions for these cases. In the computations that were performed for the present work, the default values for C_P were used. The assignment of the values of FLG_{lt} is done first for the grid points on solid walls of the configuration.

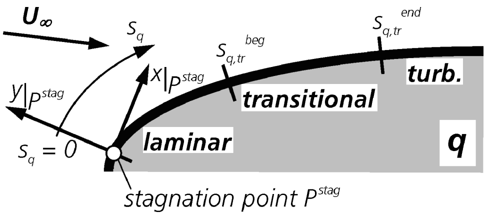

Fig. 2 Stylized depiction of laminar, transitional, and turbulent flow regions at surface side *q*.

The laminar length on the upper or lower sides of an airfoil is defined by the interval between the stagnation point and the transition point on the side q, with $q = \text{upp, low}$ indicating either the upper or the lower side of the airfoil, $0 \le s_q \le s_{q,\text{tr}}^{\text{beg}}$, where s_q is the arc length on the side q starting at the stagnation point. The turbulent length is defined by the interval between the ending point of the transitional region and the trailing-edge point on side q, $s_{q,\text{tr}}^{\text{end}} \le s_q \le s_q^{\text{trail}}$, and the transitional length is the interval between the transition point and the ending point of the transitional region, $s_{q,\text{tr}}^{\text{beg}} \le s_q \le s_{q,\text{tr}}^{\text{end}}$. The different intervals are depicted in Fig. 2.

Here γ is expressed as

$$\gamma(x) = 1 - \exp(-0.412\xi^2) \tag{10}$$

with

$$\xi = \left(x - x_{\text{tr}}^{\text{beg}}\right)\big/\lambda \tag{11}$$

according to Ref. 22, where x is the longitudinal coordinate of a flat plate with its origin located at the upstream end of the plate and λ being a measure of the extent of the transitional region. According to Ref. 13, the ending point of the transitional region $x_{\text{tr}}^{\text{end}}$ can be defined as

$$x_{\text{tr}}^{\text{end}} = x(\gamma = 0.99) \tag{12}$$

which yields

$$\lambda = \frac{\left(x_{\text{tr}}^{\text{end}} - x_{\text{tr}}^{\text{beg}}\right)}{3.36} \tag{13}$$

For the determination of the extent of the transitional region, the transition length $l_{\text{tr}} = x_{\text{tr}}^{\text{end}} - x_{\text{tr}}^{\text{beg}}$, the formulas from Ref. 23,

$$Re_{l_{\text{tr}}} = 5.2\left(Re_{x_{\text{tr}}^{\text{beg}}}\right)^{\frac{3}{4}} \tag{14}$$

for flows without pressure gradient, and

$$Re_{l_{\text{tr}}} = 2.3\left(Re_{\delta_{\text{tr}}^{*\text{beg}}}\right)^{\frac{3}{2}} \tag{15}$$

for flows with pressure gradient, are applied, as is recommended in Ref. 13 for flows in which transition does not occur before laminar separation. Whereas Eq. (14) is applied, when a laminar transition point is determined by the RANS code during the transient phase of the computation, Eq. (15) is used, when the transition prediction module has analyzed the laminar boundary layers and the

e^N-database method has not found a transition point as a result of Tollmien–Schlichting instabilities upstream of the current laminar separation point, determined by the laminar boundary-layer method. In this case, the laminar separation point from the laminar boundary-layer code is used as an approximation of the real transition point, and transition is fixed there. In all computational tests, the laminar separation point determined by the laminar boundary-layer method has always been located upstream of the laminar separation point determined by the RANS code, and the computational results using the laminar separation point from the boundary-layer method compared slightly better with experimental values than those using the laminar separation point from the RANS code.

For a predicted transition point that is determined by the e^N-database method, the formula

$$Re_{l_{\text{tr}}} = 4.6\left(Re_{\delta^{*\text{beg}}_{\text{tr}}}\right)^{\frac{3}{2}} \tag{16}$$

according to Ref. 16 is applied. Here and in Eq. (15)

$$\delta^*(x) = \int_0^{\delta(x)} \left[1 - \frac{(\rho U)(y)}{\rho_e U_e}\right] \mathrm{d}y \tag{17}$$

The thickness of the laminar boundary layer δ is evaluated according to a procedure described in Ref. 4. Thus δ^* and ρ_e and U_e, the values of the density and the tangential flow velocity at the boundary-layer edge, can be determined.

For the implementation in the RANS solver, the x coordinate in the formulas is replaced by the arc length s. Here $s_{q,\text{tr}}^{\text{beg}}$ is given either by the location of a laminar separation point, for formula a or formula b, or by a predicted transition point, for formula c, and $s_{q,\text{tr}}^{\text{end}}$ is determined by formula a, based on Eq. (15), formula b, based on Eq. (14), or formula c, based on Eq. (16), respectively. Formula a reads

$$s_{q,\text{tr}}^{\text{end(a)}} = 2.3\sqrt{(U_e/\nu_e)_{s_{q,\text{tr}}^{\text{beg}}}}\left(\delta^*_{s_{q,\text{tr}}^{\text{beg}}}\right)^{\frac{3}{2}} + s_{q,\text{tr}}^{\text{beg}} \tag{18}$$

Formula b reads

$$s_{q,\text{tr}}^{\text{end(b)}} = 5.2\left[(U_e/\nu_e)_{s_{q,\text{tr}}^{\text{beg}}}\right]^{-\frac{1}{4}}\left(s_{q,\text{tr}}^{\text{beg}}\right)^{\frac{3}{4}} + s_{q,\text{tr}}^{\text{beg}} \tag{19}$$

Formula c reads

$$s_{q,\text{tr}}^{\text{end(c)}} = 4.6\sqrt{(U_e/\nu_e)_{s_{q,\text{tr}}^{\text{beg}}}}\left(\delta^*_{s_{q,\text{tr}}^{\text{beg}}}\right)^{\frac{3}{2}} + s_{q,\text{tr}}^{\text{beg}} \tag{20}$$

and the intermittency function γ is applied in the form

$$\gamma(s_q) = 1 - \exp\left[-0.412\left(3.36\frac{s_q - s_{q,\text{tr}}^{\text{beg}}}{s_{q,\text{tr}}^{\text{end}} - s_{q,\text{tr}}^{\text{beg}}}\right)^2\right] \tag{21}$$

After all of the surface points on upper and lower side of an airfoil have been assigned to either the corresponding laminar, turbulent, or transitional interval, the field points, all points apart from the solid walls, are treated in the following way.[11] Within a limiting wall-normal distance that can be adjusted by the user of the code, every field point P_F assumes the flag value of the surface point P_S^{nst} that is located nearest to P_F,

$$FLG_{\text{lt}}(P_F) = FLG_{\text{lt}}\left[P_S^{\text{nst}}\quad(P_F)\right] \tag{22}$$

By this treatment, a laminar and a transitional zone for the current element are generated within the turbulent remainder of the computational grid. A partitioning into pure laminar zones within the turbulent remainder of the flow domain (point transition) is shown in Fig. 3. All of the steps of this procedure must be applied to all elements n_e, $1 \leq \text{n}_e \leq N_{e,}$ of the configuration for which transition prediction is performed. The order of the elements within the procedure is irrelevant.

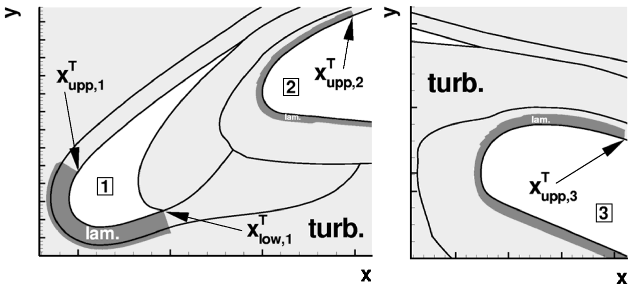

Fig. 3 Laminar zones of a two-dimensional three-element airfoil configuration in a turbulent remainder of the flow domain, point transition, slat and main airfoil (left), flap (right).

III. Computations

A. Test Cases

The test cases used to investigate the automated transition prediction functionality of the coupled system are the two-dimensional three-element takeoff and landing configurations of a representative civil aircraft consisting of slat, main airfoil, and flap.[24–27] Each configuration was considered for a low and a high Reynolds number. The structured computational grid[26] consists of about 80,000 grid points in nine blocks. The configuration has sharp trailing edges on the lower sides of the slat and the main airfoil and blunt trailing edges on the slat and main airfoil upper sides and at the end of the flap. The turbulence models used are the Spalart–Allmaras one-equation model[28] with Edwards and Chandra modification[29] (SAE) for the takeoff case and the standard Wilcox k-ω two-equation model[30] for the landing case. The turbulence models used were chosen according to Ref. 15. As shown in Refs. 11 and 31, the values of the predicted transition locations are almost not influenced by the turbulence model used in the RANS solver when the present transition prediction approach—RANS solver, laminar boundary-layer code, and e^N transition prediction—is applied. Thus, the use of different turbulence models for the validation of the applied transition prediction procedure is supposed to be justified.

The aerodynamic parameters used in the computations are $M_\infty = 0.22$, $\alpha = 21.4$ deg, $Re_\infty = 6 \times 10^6 = Re^{\text{lo}}$, and $Re_\infty = 16.8 \times 10^6 = Re^{\text{hi}}$ for both configurations. For the e^N-database method[6] the value of the limiting N factor $N|_{x^T}$ of the ONERA F1 wind tunnel, where the measuring of the wind-tunnel model had been carried out,[27] was set to $N|_{x^T} = 9$ according to Ref. 17. There the $N|_{x^T}$ value of the F1 wind tunnel was determined using the same tools as for the work presented in this paper based on an experimental pressure distribution of a single-element airfoil, which also was measured in the F1 wind tunnel. On the upper side of this pressure distribution, the transition location caused by a Tollmien–Schlichting instability is clearly recognizable by a significant pressure perturbation in the middle of an almost constant portion of the upper-side pressure distribution over the smooth airfoil surface.[17] All computations were started with initially set transition locations at 95% of the particular element's chord length, $x_{\text{tr,elem}}^{\text{init}}/c_{\text{elem}} = 0.95$ with elem = slat, main or flap, on upper and lower sides. To prevent difficulties that might arise as a result of a movement of the stagnation point in the transient phase of the computation,[14] all computations were initialized with solutions of a certain convergence level from computations with fixed transition locations, where the values of the upper-side transition points have been reasonably guessed $x_{\text{tr,elem}}^{\text{fixed}}/c_{\text{elem}} \approx 0.2$ for the takeoff case and $x_{\text{tr,elem}}^{\text{fixed}}/c_{\text{elem}} \approx 0.1$ for the landing case; the lower side transition points were fixed at $x_{\text{tr,elem}}^{\text{fixed}}/c_{\text{elem}} = 0.95$ on all elements for all of these cases. In the transition prediction iteration, the RANS cycle interval between two consecutive calls of the transition prediction module was set to $\Delta k_{\text{cyc}} = 2000$, and for the RANS computations a three-level multigrid method was applied. The experimental data are taken from Ref. 27.

B. Results

The computations of all cases result in a flow structure that is typical for an aircraft multielement high-lift configuration before maximum lift. The flow is fully attached on the lower sides of the slat, the main airfoil, and the flap. In the coves of the main airfoil and of the slat, separation bubbles are located. The separation bubble in the slat cove is significantly smaller in the computations with transition than in fully turbulent computations. The c_p distribution on the slat upper side is characterized by a high suction peak in all cases. On the upper sides of the main airfoil and the flap, the c_p distributions show spiky perturbations coming from the contour kinks where the trailing edges of the slat and the main airfoil are located when the configuration is undeflected. In all cases, the results of the computations yield that on the lower sides of the slat, the main airfoil and the flap the flow remains fully laminar from the stagnation point up to the intitially set lower transition points at 95%.

The Re^{lo}-takeoff case exhibits a stationary separation bubble on the rear 14% of the main airfoil upper side, in contrast to the Re^{hi}-takeoff case, where the flow is fully attached. For both cases the flow on the flap and slat upper sides is fully attached. For both Reynolds numbers, the flow over the landing configuration is characterized by trailing-edge separation bubbles on the upper sides of the slat and the flap. The extent of the slat separation bubble is about 4% of the slat chord length in the Re^{lo}-landing case and about 10% in the Re^{hi}-landing case. For both Reynolds numbers, the extent of the flap separation bubble is about 16% of the flap chord length.

1. *RANS Convergence Histories*

A monitoring of the separation points of the two landing configuration shows that for both Reynolds numbers the slat separation point and for the Re^{lo}-landing case also the flap separation point oscillates very slightly so that the convergence of the computations, which were performed using local time stepping in order to compute steady solutions, is visibly affected. The density residual leveled out at an average value of about 10^{-2}. The convergence histories of the density residual, the lift coefficient c_l, and the drag coefficient c_d are oscillating around steady average values. For c_l and c_d, the corresponding steady average values are supposed to represent the steady-state values. In Fig. 4 this behavior is depicted for the Re^{lo}-landing case. The dotted line at cycle ≈ 6000 marks the situation directly after the restart using the restart solution with fixed transition locations; here the transition prediction procedure with initial transition locations, which were set almost at the trailing edges, starts. The final step of the transition location iteration is done at the cycle marked with a dashed line. Apart from the oscillations in the curves of the force coefficients, the convergence histories are very smooth, and after the first part of the transient phase where perturbations are well damped all evolution tendencies are clear. The behavior of the Re^{hi}-landing case is very similar.

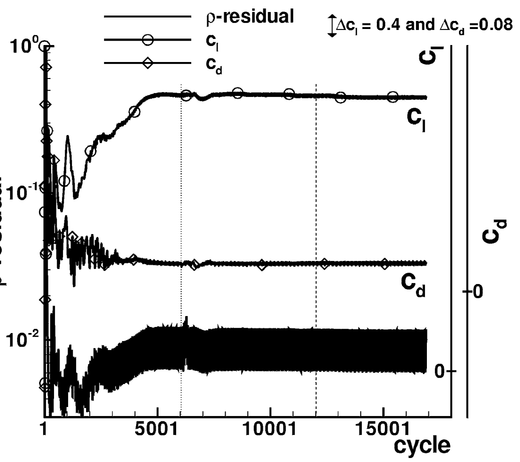

Fig. 4 Convergence history of the RANS computation, low-Reynolds-number landing case: . . . . , transition prediction start; - - - -, transition prediction end.

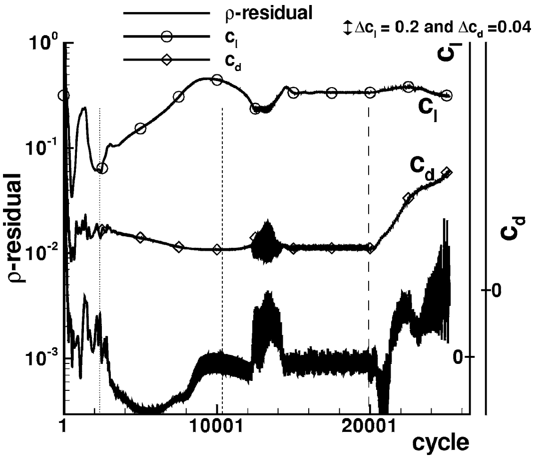

Fig. 5 Convergence history of the RANS computation, low-Reynolds-number takeoff case: . . . . , transition prediction start; - - - -, transition prediction end; — — —, start of unsteady computation.

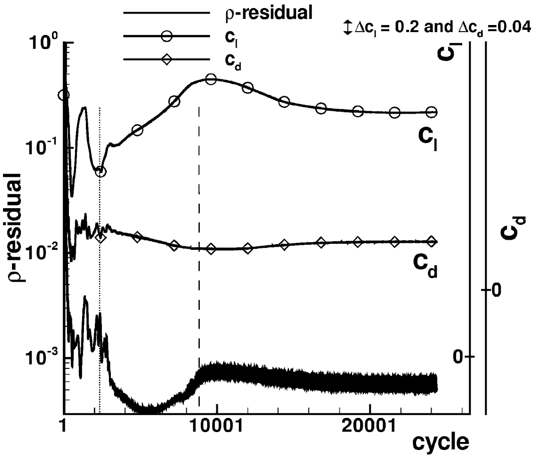

Fig. 6 Convergence history of the RANS computation, low-Reynolds-number takeoff case: . . . . , here the transition prediction process had started; — — —, here the restart run started using fixed predicted transition locations.

For the takeoff cases, the convergence stage of the restart solutions was of very different character. After about 2350 RANS cycles, the convergence stage of the computations with fixed, guessed transition locations has reached a state where one can expect that the movement of the stagnation points on all elements has stopped. This cycle is marked by the dotted line in Fig. 5 for the Re^{lo}-takeoff case. Thus, in the transition prediction iteration the setting of $\Delta k_{\mathrm{cyc}} = 2000$ provokes calls of the transition prediction module in a situation where the lift coefficient c_l has not yet converged. However the convergence history of the lift coefficient is smooth, and its evolution tendency is clear in these situations so that one can expect reasonable results from the transition prediction module anyhow. The dashed line marks the situation when the transition prediction module was called for the fourth and last time at cycle $\approx 10{,}350$. The continuing computation, where the transition locations do not change anymore, is strongly perturbed and ends up with spiky oscillations in both the curves of the density residual and the force coefficients. The attempt to obtain a steady solution from an unsteady computation—marked by the long dashed line in Fig. 5—using a dual-time-stepping scheme[10,21] also failed. In Fig. 6, the convergence histories are shown for a computation, which was started with a restart solution from cycle ≈ 8850. In this situation, the force coefficients have reached a state of convergence, where their values changed only slightly during the last 850 cycles and the value of the density residual is sufficiently small. Thus, one can expect that the numerical disturbances which have remained in the restart solution are well damped in the new computation, which was performed using the transition locations that were predicted by the transition location iteration before. Now, the convergence histories are very smooth, do not show any perturbations, and end up in a

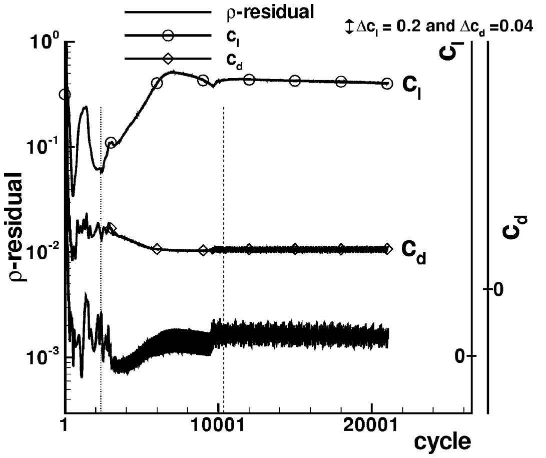

Fig. 7 Convergence history of the RANS computation, high-Reynolds-number takeoff case: . . . . , transition prediction start; - - - -, transition prediction end.

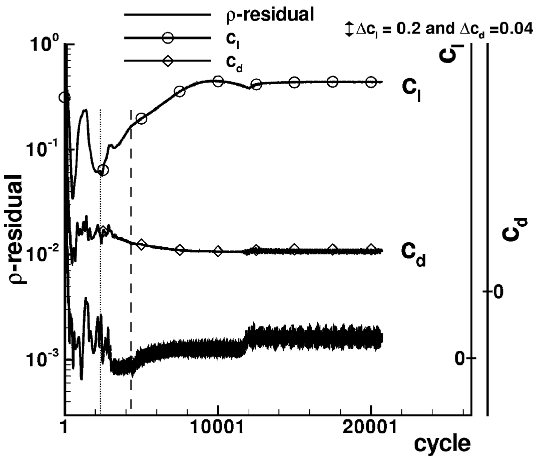

Fig. 8 Convergence history of the RANS computation, high-Reynolds-number takeoff case: . . . . , here the transition prediction process had started; – – –, here the restart run started using fixed predicted transition locations.

steady solution based on a steady computation. Figures 7 and 8 show a similar behavior of Re^{hi}-takeoff case. In this case however, it was necessary to restart the computation based on a flowfield solution from a very early convergence stage where the value of the density residual is sufficiently small (Fig. 8). Finally, the very smooth lift convergence curve reaches a steady state, and the drag is oscillating around a steady average value.

For the two takeoff cases, there seems to exist an interaction between the transition prediction iteration, the level of the numerical disturbances, which have remained in the solution, and the separation bubbles, which evolve at the main airfoil trailing edge during the computations. In both cases, the separation bubbles start to evolve and to grow before the transition location iteration has converged. In this part of the transient phase of the computations, the numerical disturbances (represented by the density residual) are oscillating with high amplitudes, and their average value is slightly decreasing. When the separation bubbles have reached a certain extent, they become unsteady, the numerical disturbances are excited, and the extent of the bubbles decrease until they have reached stable average values. The separation bubbles remain unsteady, and also the excited disturbances stay in the unsteady solutions of the steady computations. For the Re^{lo}-takeoff case, this behavior is strongly pronounced. Thus, the attempt to reduce the overall computation time by starting the transition location iteration at an early stage of the RANS computation has failed.

2. *Transition Locations*

In Figs. 9–12, the convergence of the transition location iterations on the upper sides of the slat, the main airfoil, and the flap for all test cases are depicted, and the converged values are compared to experimental data as far as they are available. This is the case for the slat and the flap for all test cases.[27] In the figures the transition location values that come directly from the transition prediction module are depicted by dashed lines and the underrelaxed values by solid lines. A laminar separation point from the RANS computational grid, which is used as a transition point, is depicted by a square hollow symbol while a laminar separation point from the laminar

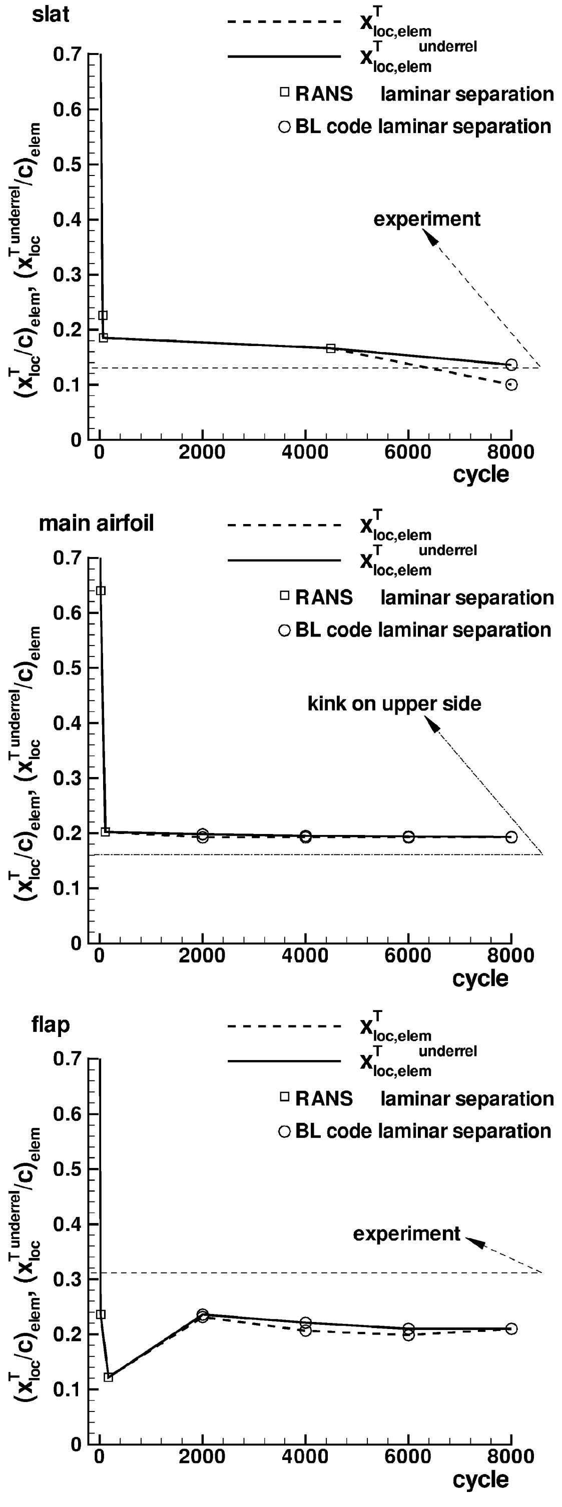

Fig. 9 Convergence histories of the transition location iteration at the slat, main airfoil, and flap, low-Reynolds-number takeoff case.

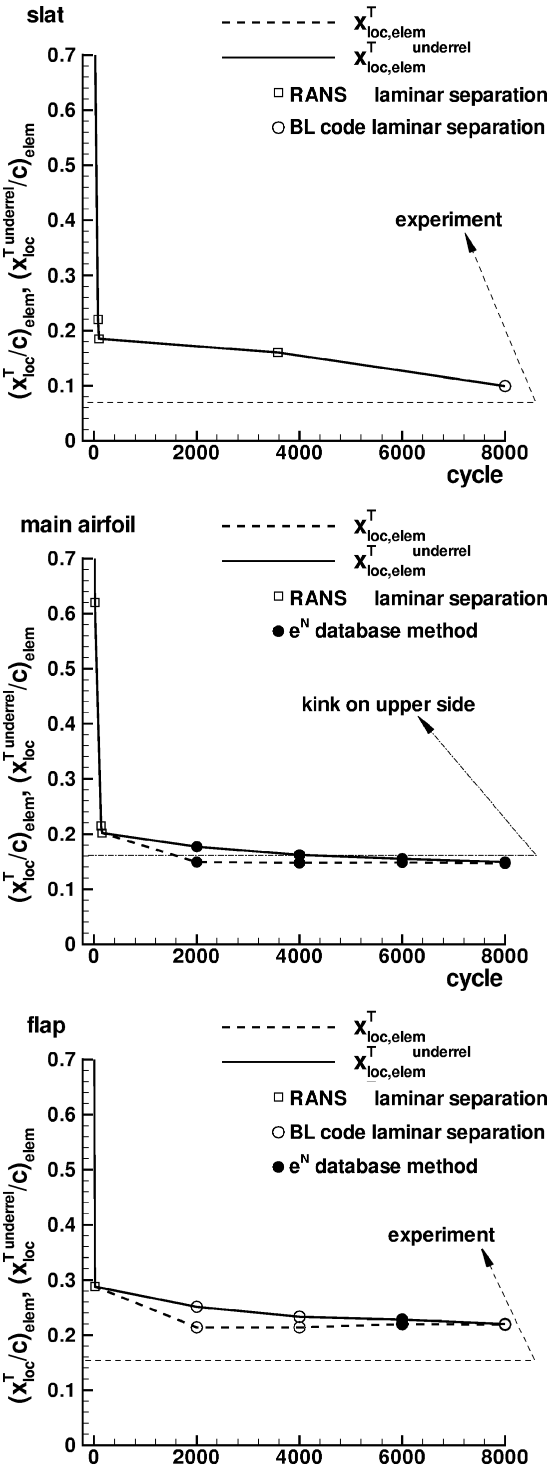

Fig. 10 Convergence histories of the transition location iteration at the slat, main airfoil, and flap, high-Reynolds-number takeoff case.

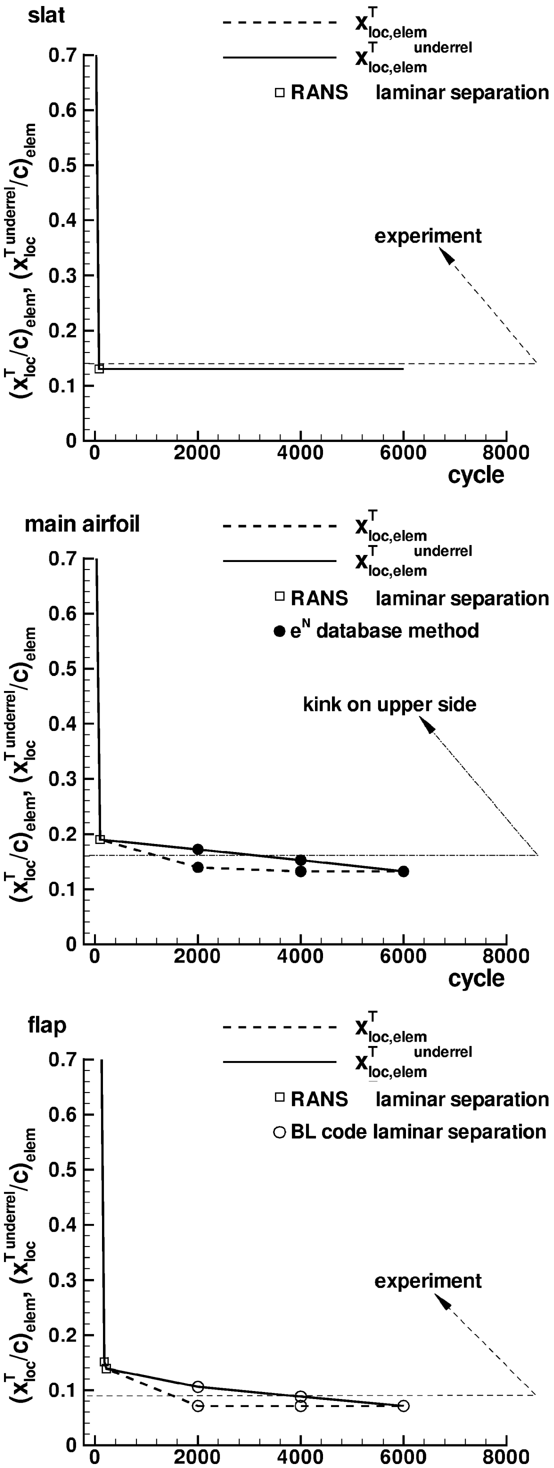

Fig. 11 Convergence histories of the transition location iteration at the slat, main airfoil, and flap, low-Reynolds-number landing case.

boundary-layer code is depicted by a circular hollow symbol. A transition point caused by Tollmien–Schlichting instabilities detected by the e^N-database method is depicted by a black circular symbol. The values of the experimentally determined transition locations are marked by thin dashed lines. For the main airfoil, the location of the upper-side kink is marked by a dashed-dotted line because transition is expected to occur in the vicinity of this location. The values of the transition points are normalized with respect to the chord length of the corresponding element and are plotted against the RANS iteration cycles. Iterations start at cycle $= 0$, which corresponds to the beginning of the computation, with transition prediction based on the restart solution from the computation with fixed, guessed transition locations. For the takeoff cases, four steps of the transition location iteration are needed until the values of the transition points have converged. Because of the different convergence state of the restart solution, for the landing cases only three iteration steps are needed.

At the Re^{lo}-takeoff configuration, all transition points that occur in the transition prediction iteration are based on laminar separations during the transient phase of the computation (Fig. 9). All converged values come from the laminar boundary-layer method and yield an excellent approximation at the slat, a value in the area

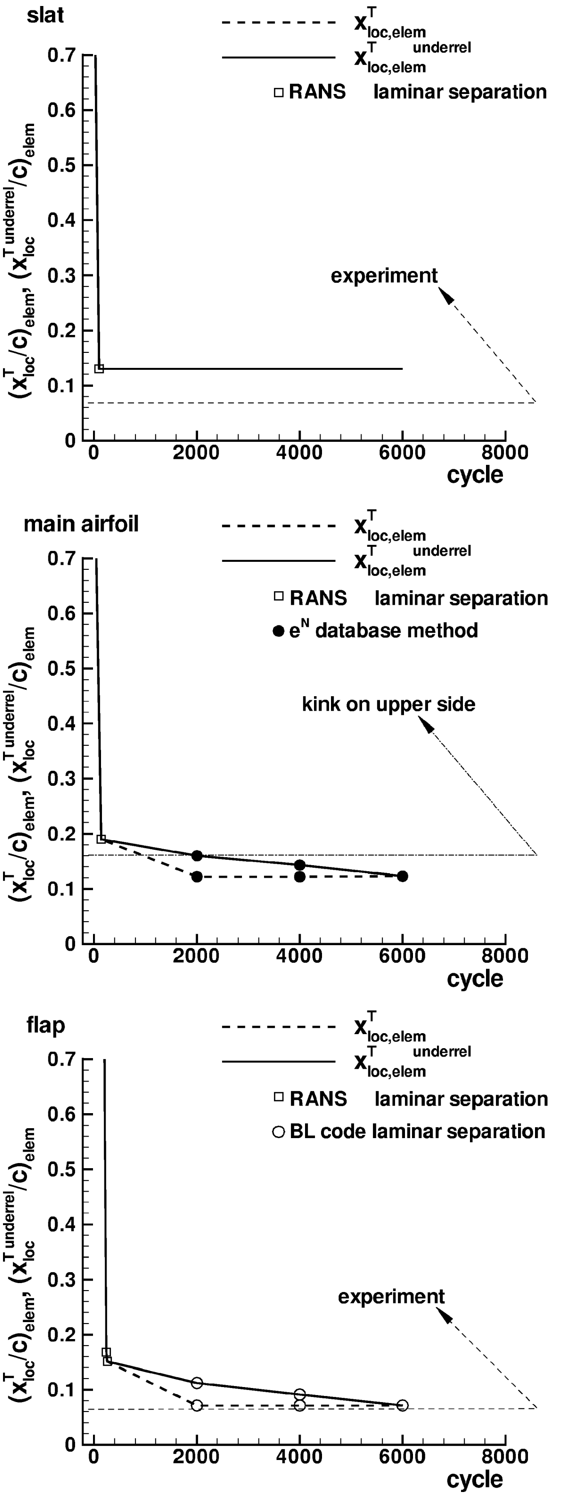

Fig. 12 Convergence histories of the transition location iteration at the slat, main airfoil, and flap, high-Reynolds-number landing case.

where transition is expected at the main airfoil, but a bad approximation at the flap where the predicted transition point is located too far upstream. For the upper-side flap transition point, the approach of using the laminar separation point as an approximation of the real transition point fails when transition does not occur before the laminar boundary layer separates. In any case, a more capable transition prediction approach that is able to detect the transition point downstream of the point of laminar separation is needed here. However, also the quality of the reported transition location from the experiment[27] can be questioned. In Ref. 27 an error interval for the transition location measurements—the transition detection was based on infrared thermography—on the flap is given, which has a size of 1.2% of the chord length of the flap.

For the Re^{hi}-takeoff configuration, the converged values come from the laminar boundary-layer method at the slat and the flap and from the e^N database method at the main airfoil (Fig. 10), and yield a very good approximation at the slat, a value in the area where transition is expected at the main airfoil and a tolerable approximation at the flap. Here, it seems to be clear that transition did not occur as a result of Tollmien–Schlichting waves because one should have a value of the limiting N factor of $N|_{x^T} \approx 0.5$ to obtain the experimental value from the e^N database method. This value of the limiting N factor $N|_{x^T}$ is definitely too small.[17,18] Here it might be possible that turbulent disturbances emanating from the main element wake affect the upper-side boundary layer of the flap[32] and lead to a type of bypass transition or confluent wake/boundary instability.[33] The application of criteria for this type of bypass transition can yield a better approximation here.

Figure 11 shows the results for the Re^{lo}-landing configuration. At the slat the final transition point comes from a laminar separation point detected in the RANS computational grid, instead from the laminar boundary-layer code, which is normally the case. This is because usually the prediction of laminar flow separation is more conservative in RANS methods compared to laminar flow separation prediction by boundary-layer methods, which indicate laminar separation at a position further upstream. At first sight this result is surprising, but it is an effect that is purely based on the details of the underrelaxation technique. The laminar separation point from the boundary-layer code in the last step of the transition location iteration is $x_{\mathrm{sep,slat}}/c_{\mathrm{slat}} \approx 0.091$, but it is not taken into account by the underrelaxation algorithm as a result of the underrelaxation parameter settings for the slat. At the main airfoil, the converged value is caused by Tollmien–Schlichting waves and is located in the area where transition is expected. At the flap it is approximated by a laminar separation point from the boundary-layer code. The quality of the approximation at the slat and the flap is good.

Finally, the results of the Re^{hi}-landing configuration are shown in Fig. 12. At the slat the final transition point comes from a laminar separation point detected in the RANS computational grid, for the same reason as for the Re^{lo}-landing configuration. In contrast to the Re^{lo}-landing configuration where the final transition point is located a little bit too far upstream compared to the experimental value (which results in an approximation better than if the laminar separation point from the boundary-layer code had been used), the final transition point is located significantly too far downstream of the experimental value. Furthermore, the laminar separation point from the boundary-layer code, which is located at $x_{\mathrm{sep,slat}}/c_{\mathrm{slat}} \approx 0.097$, gives a very good approximation of the experimental value. This leads to the conclusion that for the fully automatic transition prediction procedure—a better approximation of the transition location on the slat is also possible by the manual input of the laminar separation point from the boundary-layer code of course—the underrelaxation parameter settings must be very carefully adjusted on the one hand. On the other hand, it becomes evident that it is necessary to account for transition downstream of the point of laminar separation in order to get good results on the slat of the landing configuration in both cases. At the main airfoil, the converged value of the transition point is caused by Tollmien–Schlichting waves, and it is located in the area where transition is expected. At the flap it is approximated by a laminar separation point from the boundary-layer code. The quality of the approximation at the flap is almost perfect.

An overview of the computed values of the transition locations $(x_{\mathrm{tr}}/c)_{\mathrm{elem}}$ and the agreement with the experimental values according to

$$\Delta x_{\mathrm{tr,elem}} = \left(x^{\mathrm{comp}}_{\mathrm{tr,elem}} - x^{\mathrm{exp}}_{\mathrm{tr,elem}}\right) \Big/ c_{\mathrm{elem}} \tag{23}$$

is shown in Table 1, where for the main airfoil the location of the transition point relative to the upper-side kink is given.

In Table 2, the corresponding transition lengths $(l_{\mathrm{tr}}/c)_{\mathrm{elem}}$, which should be in the order of magnitude of about 5% of the chord length of the particular element $l_{\mathrm{tr,elem}} = 5\%\ \mathrm{c}_{\mathrm{elem}}$, are given.

Table 1 Computed values of the transition locations $(x_{tr}/c)_{elem}$ at slat, main airfoil, and flap and agreement with the experimental values (For the main airfoil the transition location relative to the upper-side kink is given.)

	Takeoff				Landing			
	Re^{lo}		Re^{hi}		Re^{lo}		Re^{hi}	
Elem	$(x_{tr}/c)_{elem}$	$\Delta x_{tr,elem}$, %	$(x_{tr}/c)_{elem}$	$\Delta x_{tr,elem}$, %	$(x_{tr}/c)_{elem}$	$\Delta x_{tr,elem}$, %	$(x_{tr}/c)_{elem}$	$\Delta x_{tr,elem}$, %
Slat	0.136	0.45	0.099	3.1	0.13	−1.05	0.13	6.23
Main	0.193	3.24	0.149	−1.16	0.132	−2.86	0.123	−3.76
Flap	0.2098	−10.3	0.22	6.57	0.071	−1.86	0.071	0.7

Table 2 Computed values of the transition lengths $(l_{tr}/c)_{elem}$ at slat, main airfoil, and flap

	Takeoff		Landing	
Elem	$(l_{tr}/c)_{elem}$ for Re^{lo}, %	$(l_{tr}/c)_{elem}$ for Re^{hi}, %	$(l_{tr}/c)_{elem}$ for Re^{lo}, %	$(l_{tr}/c)_{elem}$ for Re^{hi}, %
Slat	6.76	4.75	6.94	5.37
Main	3.57	5.08	7.01	5.35
Flap	4.87	3.96	3.16	2.7

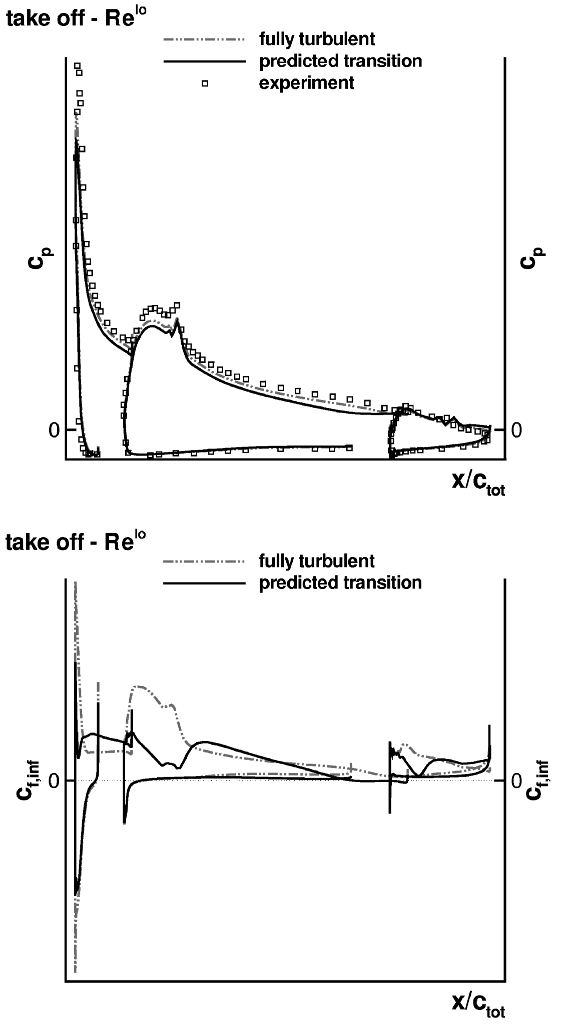

Fig. 13 The c_p and c_f distributions, low-Reynolds-number takeoff case, SAE turbulence model.

3. Pressure and Skin-Friction Distributions

In Figs. 13–16, the c_p and c_f distributions of the four cases are shown. The c_p distribution of the Re^{lo}-takeoff case (Fig. 13) quantitatively does not agree well with the experimental one on the slat and the main airfoil and even exhibits higher deviations than the c_p distribution of a fully turbulent computation, especially in the upper-side suction peak areas. This is an unexpected result and can be explained with the existence of the trailing-edge separation bubble at the main airfoil upper side, which does not appear in the fully turbulent computation. For the Re^{hi}-takeoff case (Fig. 14) the agreement of experimental and computed c_p distributions is much better. Although also in this case the suction peak at the slat is not reached, the overall agreement is satisfying. The c_p distributions of the fully turbulent computation and the computation with transition are almost the same, and even the c_f distributions of both computations match in large portions of the main airfoil and the flap. On the upper sides of both components, the minimum c_f values in the transitional flow regions are the same, and they are located at the same positions. The c_f rise in the transition region of the main airfoil is more abrupt in the fully turbulent case than in the case with transition locations and transition lengths, and at the flap the computed c_f distributions are almost identical. In this high-Reynolds-number case, the turbulence model used is able to simulate laminar flow and transition to turbulence without having prescribed laminar flow regions in the computational grid, for two of the three components of the

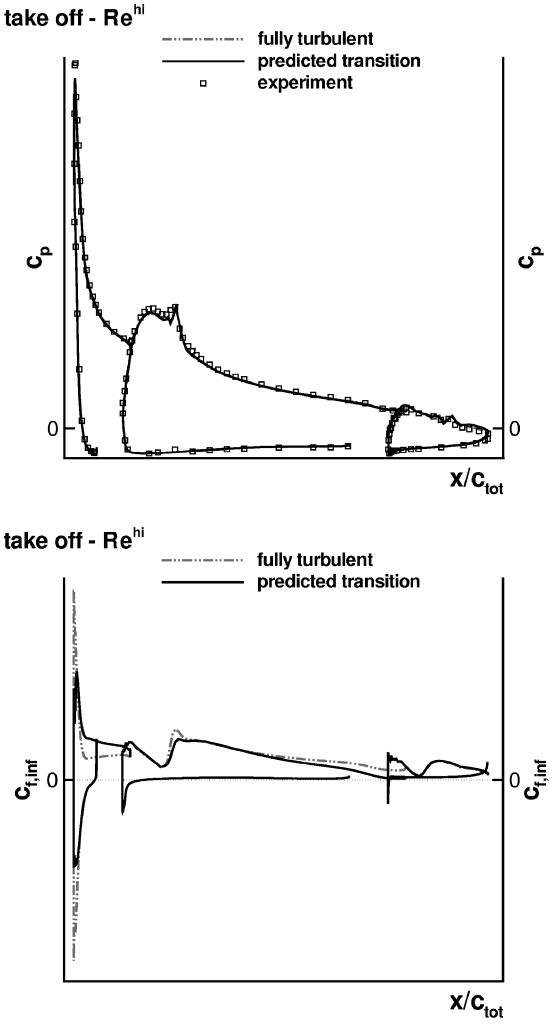

Fig. 14 The c_p and c_f distributions, high-Reynolds-number takeoff case, SAE turbulence model.

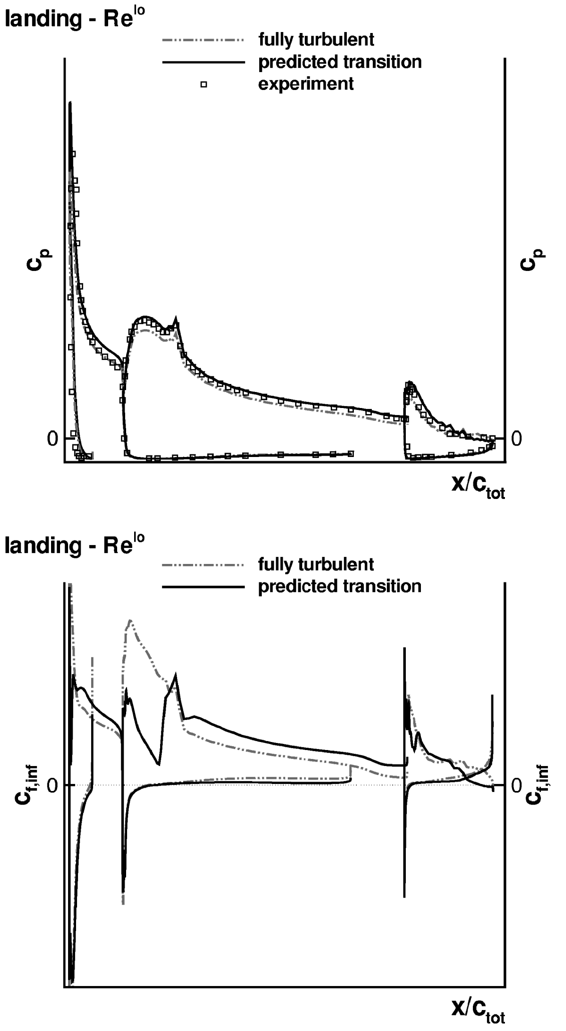

Fig. 15 The c_p and c_f distributions, low-Reynolds-number landing case, Wilcox k-ω turbulence model.

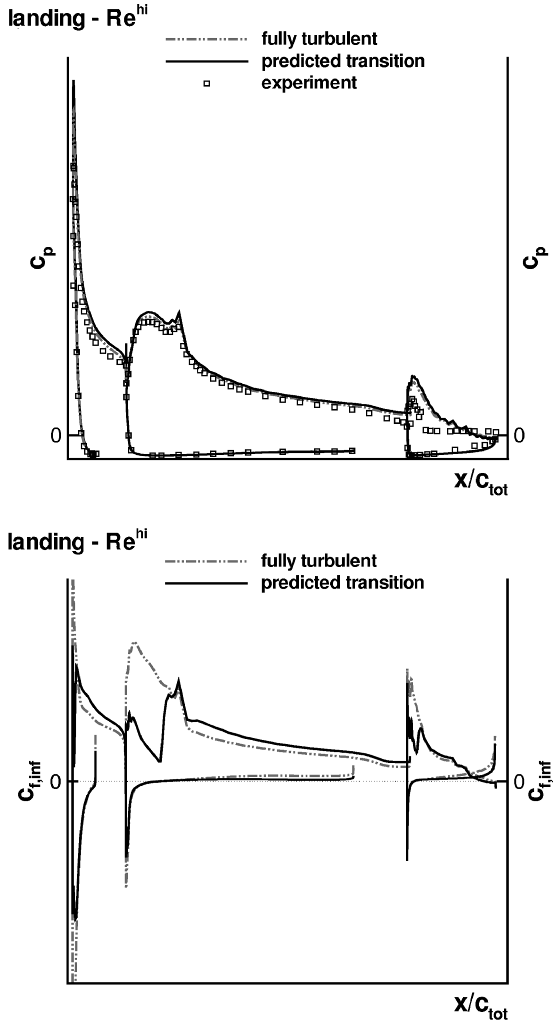

Fig. 16 The c_p and c_f distributions, high-Reynolds-number landing case, Wilcox k-ω turbulence model.

configuration. This behavior can be caused by the high Reynolds number (and the corresponding low value of the molecular viscosity), which has a damping influence on the turbulence production term of the SAE model. The results of the computation with transition show that on the main airfoil upper side the flow is very near to separation at the trailing edge in contrast to the fully turbulent results.

Figure 15 shows the results for the Re^{lo}-landing case. Here, a clear improvement with respect to the predicted c_p distributions on the main airfoil and in the suction area of the flap is obtained in the computation with transition. The suction peak on the slat is overestimated in the computation with transition, whereas in the fully turbulent computation the suction peak is not reached. The flap separation bubble in the computation with transition leads to a slight underestimation of the pressure level at the flap trailing edge. At the main airfoil, the turbulent skin-friction level is significantly higher in the computation with transition than in the fully turbulent computation. Finally, in Fig. 16 the results for the Re^{hi}-landing case are depicted. Here both the computation with transition and the fully turbulent computation clearly overestimate the suction peak at the slat, and in both cases the large separation bubble on the flap upper side, which is clearly visible in the experimental c_p distribution, is not predicted. This leads to an overestimation of the overall c_p level on all elements. The differences between the results from the computation with transition and the fully turbulent computation are as expected for the c_p distributions as well as for the c_f distributions.

Because the computational results for the takeoff configuration using the SAE turbulence model were not of sufficient quality with respect to the accuracy of the predicted pressure distributions, the computations were repeated applying the Wilcox k-ω turbulence model using the transition locations and transition lengths determined in the SAE computations. The computational results are shown in the Figs. 17 and 18. Now, for both Reynolds numbers, the suction peaks at the slat, and for the low Reynolds number the experimental pressure level on the slat upper side, are reached with very good accuracy. The pressure levels on the main airfoil upper side are improved visibly in both cases. The improvement for the low-Reynolds-number case is significant. The deviations between the experimental and the computed c_p distributions at the flap almost do not appear anymore. Remarkable are the differences in the c_f distributions, especially in the transition regions. In both computations using the Wilcox k-ω model, the c_f rise directly downstream of the transition point occurs more rapidly and more intensely for all three elements than in the computations using the SAE model, and the local maximum c_f value at the beginning of the fully turbulent flow region is greater. In both cases, the turbulent boundary layer at the upper-side trailing edge of the main airfoil is far from separation with the Wilcox k-ω model.

To verify if the unsatisfactory results using the SAE model originate from the application of the transition lengths and the intermittency function, the computations with the SAE model were repeated using the same transition locations but applying point transition instead of the transitional flow models. In both cases, the c_p distributions are almost the same as the ones with transitional flow models. The c_f distributions for the Re^{lo} takeoff case are almost the same as for the case with transitional flow models at the slat and the main airfoil. At the flap the c_f rise directly downstream of the

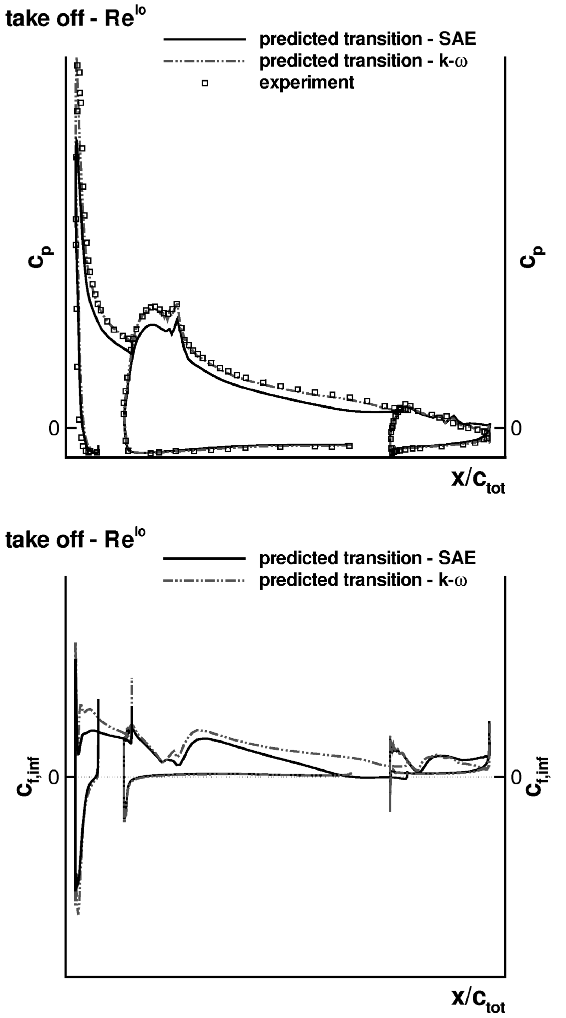

Fig. 17 The c_p and c_f distributions, low-Reynolds-number takeoff case, Wilcox k-ω turbulence model.

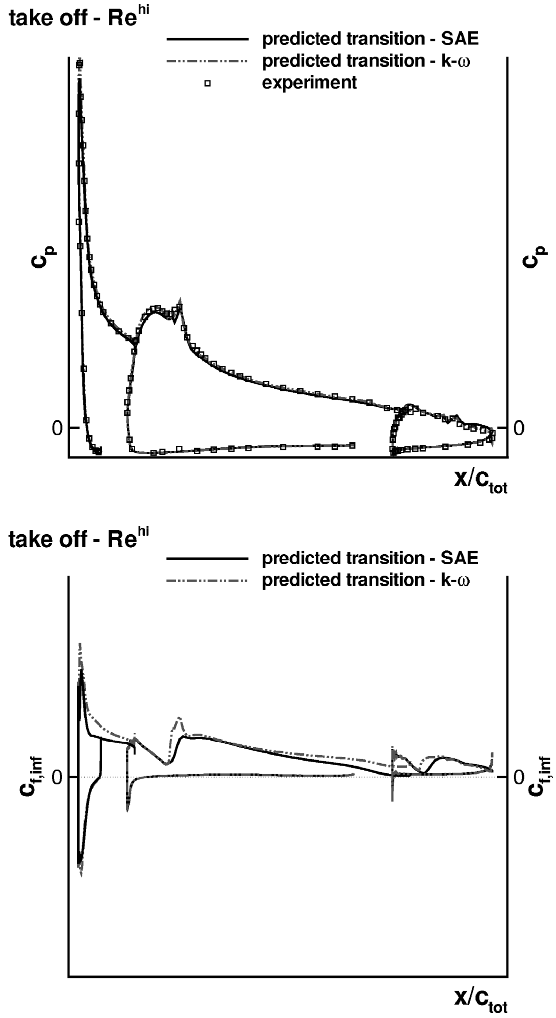

Fig. 18 The c_p and c_f distributions, high-Reynolds-number takeoff case, Wilcox k-ω turbulence model.

transition point starts a bit sooner, than in the case with transitional flow models. For the Re^{hi}-takeoff case, at the slat and the flap the c_f distributions are almost identical to the ones from the computations with transitional flow models. At the main airfoil the c_f distribution is identical to the one from the fully turbulent computation.

This outcome indicates that the properties of the turbulence model itself are the cause for the unexpected behavior of the SAE model in the computations with predicted transition locations.

4. Lift and Drag Coefficients

Finally, an overview over the experimentally measured and computed lift coefficients c_l and drag coefficients c_d is presented in Figs. 19 and 20, where the experimental drag coefficient values were determined by far-wake surveys[27]—carried out perpendicularly to the freestream velocity—including all uncertainties that are known for far-wake drag estimates performed on high-lift configurations. Usually the far-wake drag estimates are done based on total pressures, which do not account for the very high angle of the flow downwash so that low estimates of drag values are a consequence.

Figure 19 shows this comparison for the takeoff configuration, which exhibits a trend of the experimental lift coefficient to lower values with increasing Reynolds number. This might be caused by the separation bubble at the slat that was detected for the low Reynolds number, but did not occur for the high Reynolds number.[27] A closer inspection of the c_p distributions at the slat reveals the reported difference and visibly higher suction levels over wide portions of the slat upper side for the low Reynolds number. The very unsatisfactory computed c_l values using the SAE turbulence model can be improved drastically, by using the Wilcox k-ω model and the

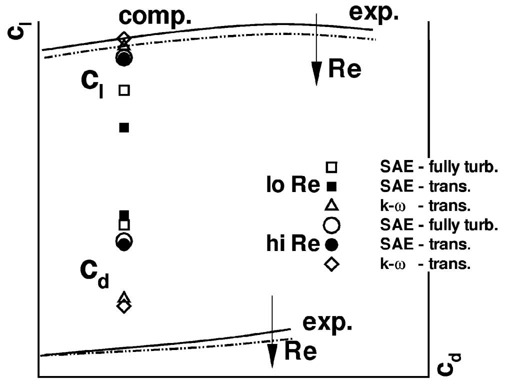

Fig. 19 Measured and computed lift coefficients c_l and drag coefficients c_d vs the angle-of-attack α takeoff case.

predicted transition locations, to results that differ from the experimental ones less then 1.5%, that is, $\Delta c_l < 1.5\%$, according to

$$\Delta c_k = \left(c_k^{\text{comp}} - c_k^{\text{exp}}\right) \Big/ c_k^{\text{exp}} \qquad k = l, d \tag{24}$$

The Reynolds-number effect for the computed lift coefficients is contrary to the experimental trend, which is understandable because in the computations no separations bubbles are predicted. Thus one gets the usual Reynolds-number effect, with higher suction levels on the slat upper side for the higher Reynolds number. The computed

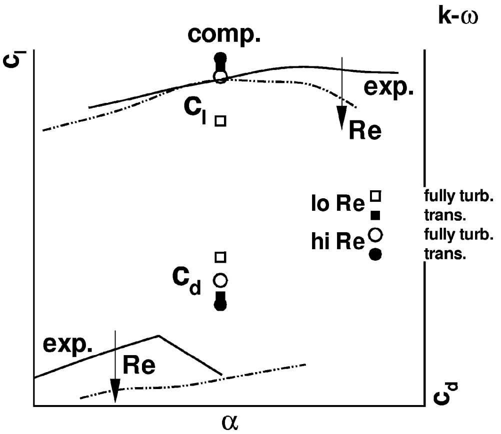

Fig. 20 Measured and computed lift coefficients c_l and drag coefficients c_d vs the angle-of-attack α landing case.

drag coefficients that differ significantly from the experimental far-wake drag estimates can be improved drastically as well when the predicted transition locations are applied, and the Wilcox k-ω model is used. The differences between the experimental and the computed drag Δc_d according to Eq. (24) decrease from over 120% for the computations with the SAE model to about 50% using the Wilcox k-ω model. The Reynolds-number effect in the computations is as it was found in the measurements. The possibility that the computed values of the drag coefficient of a high-lift configuration can deviate strongly from the experimental values is well known and reported for example in Ref. 34, where another configuration was investigated. There the comparison of the computed pressure drag with pressure drag estimates from the integrated experimental pressures yielded good results in some cases. Unfortunately, the experimental pressure drags for the configurations investigated in this work are not available. Besides the uncertainties of the experimental approach of drag estimation, which definitely contributes to the difference between the experimental and the computed drag values, the differences between the computed and the measured pressures can be a cause of the deviations. In Ref. 35, this issue was investigated in detail, and it was shown that the overall pressure drag of a high-lift configuration, which dominates the drag value of the configuration as a whole as well as the drag of every single element, is composed of a balance of very large positive and negative contributions. The contribution of one single element can be one order of magnitude larger than the resulting overall drag of the complete configuration. Thus, a relative error of 5% of the computed drag on the slat upper side can result in a change of 50% for the overall drag value.[35] At this point, as so often, the question arises: how much are the transition prediction and transition modeling on the one hand, and the turbulence modeling on the other hand, responsible for this effect, and how much do they contribute to it.[17]

For the landing configuration measurements, random occurrence of flow separation over the flap is reported for the low Reynolds number.[27] Also for the high Reynolds number, separation over the flap was observed, but here it was possible to reduce this phenomenon by cleaning the wind-tunnel model.

The experimental force coefficient values for the Re^{lo}-landing case in Fig. 20 do not correspond to the experimental c_p distribution in Fig. 15 with attached flow over the flap, but to the separated flow case whose c_p distribution is not shown in this presentation. For the Re^{hi}-landing case, the experimental force coefficient values in Fig. 20 do not correspond to the experimental c_p distribution in Fig. 16 with separated flow over the flap, but to the case with attached flow over the flap of the cleaned wind-tunnel model. The experimental c_p distribution for this flow case is compared to the one computed in Fig. 21. In this comparison, one finds a significantly improved matching of the experimental and computed c_p distributions on the flap and also on the main airfoil. At the slat however, the suction peak still seems to be highly overestimated. Moreover, the deviation of the location of the suction peak has increased visibly in this comparison, which would mean a worsening of the experimental and computed agreement, compared to the flow case with flow separation over the flap.

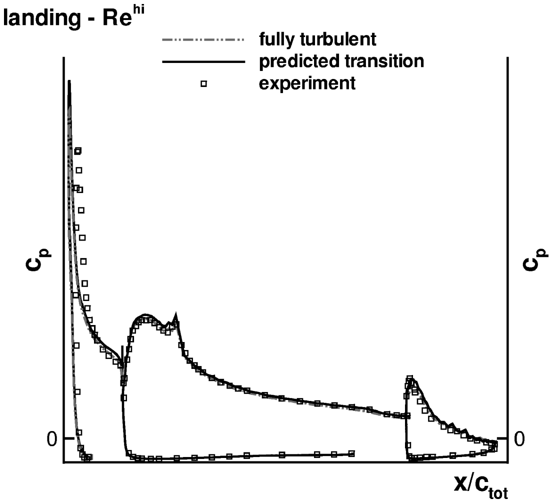

Fig. 21 The c_p distributions, high-Reynolds-number landing case, Wilcox k-ω turbulence model, experimental distribution taken at the cleaned wind-tunnel model with attached flow over the flap.

The Reynolds-number trend of the experimental lift coefficient is similar to the takeoff configuration, also the same differences with respect to the existence of the slat separation bubble are reported.[27] These are visible in a close inspection of the corresponding c_p distributions, and the same circumstance in the computations—no separation on the slat—as in the takeoff cases occurs. For the Re^{lo}-landing case, the computation with transition reduces the error in the computed lift coefficient from over 9% to less than 3%. For the Re^{hi}-landing case, the c_l value of the fully turbulent computation has an error of less than 1%, while the value of the computation with transition has an error of almost 5%. In the computations, one gets the usual Reynolds-number effect, with higher lift for a higher Reynolds number.

The differences between the experimental and the computed drag Δc_d, according to Eq. (24), decrease from about 98% for the fully turbulent computations of both cases to about 66% for the computations of both cases with transition. The Reynolds-number effect in the computations is as it was found in the measurements.

Finally it must be emphasized here that the wake measurements at the landing configuration were affected by the occurrence of the separation over the flap,[27] which led to an unsteady flow in these situations. This brings up the question of how much of the unsteadiness might have remained in the reported values of the force coefficients.

IV. Conclusions

The DLR Reynolds-averaged Navier–Stokes (RANS) solver FLOWer was coupled to the DLR transition prediction module in order to perform RANS computations of high-lift multi-element systems with automatic laminar-turbulent transition prediction. It could be shown that the coupled system represents a RANS-based computational-fluid-dynamics tool that provides accurate values of the transition locations during the ongoing RANS computation automatically and fast without the need for the intervention by the code user. Thus, RANS computations of high-lift multi-element configurations with transition can be carried out without a priori knowledge of the transition characteristics of the specific flow problem.

The transition prediction coupling procedure was successfully applied to a number of three-element high-lift test cases. The transition location iterations converge fast, and the predicted transition locations are partly of excellent accuracy. Nevertheless, in some cases the accuracy must be improved by taking into account other transition prediction approaches that are able to detect the transition point downstream of the point of laminar separation, or that detect bypass transition (confluent wake/boundary instability). All transition lengths are of the expected order of magnitude.

The comparison of the computed and the experimentally determined pressure distributions yields a good agreement for the two takeoff test cases and a satisfying agreement for the two landing cases when the Wilcox k-ω turbulence model was used. The computed lift coefficients agree well with the experimental findings. However, the computed drag coefficients show significant deviations from the experimental values. In this respect, the abilities of the turbulence models used must be questioned, and other turbulence models must be tested. Nevertheless, the results of the computations with predicted transition locations yield a significantly lower error in the computed drag values—the error decreases by about 30%—compared to the results from fully turbulent computations.

The turbulence model used can have—although it almost does not influence the results of the transition prediction procedure—a significant impact on the computed c_p and c_f distributions and on the force coefficients. The use of the same values of the transition locations and the transition lengths led to the expected improvement of the computed quantities compared to the results from fully turbulent computations in all cases when the Wilcox k-ω turbulence model was used. For one of the two cases that were computed using the Spalart–Allmaras model with Edwards and Chandra modification however, the results from the computation with transition exhibited significantly larger deviations from the experimental data than the fully turbulent computational results.

Finally, the application of more capable transition prediction approaches, and other transition criteria must be tested, and their impact on the pressure distribution and the force coefficients must be investigated. The consideration of these transition prediction issues will be addressed within the European project EUROLIFT II.

Acknowledgments

This work has partly been carried out within the HiAer Project (High Level Modelling of High Lift Aerodynamics). The HiAer project is a collaboration between DLR, ONERA, KTH, HUT, TUB, Alenia, Airbus Deutschland, QinetiQ, and FOI. The project is managed by FOI and is partly funded by the European Union (Project Ref: G4RD-CT-2001-00448). We acknowledge BAE Systems for letting us use the 59% section data of a representative civil aircraft wing in this study.

References

[1] Radespiel, R., Graage, K., and Brodersen, O., "Transition Predictions Using Reynolds-Averaged Navier–Stokes and Linear Stability Analysis Methods," AIAA Paper 91-1641, June 1991.

[2] Smith, A. M. O., and Gamberoni, N., "Transition, Pressure Gradient and Stability Theory," Douglas Aircraft Co., Rept. ES 26388, Long Beach, CA, Aug. 1956.

[3] van Ingen, J. L., "A Suggested Semi-Empirical Method for the Calculation of the Boundary Layer Transition Region," Dept. of Aerospace Engineering, Rept. VTH-74, Univ. of Delft, Delft, The Netherlands, Oct. 1956.

[4] Stock, H. W., and Haase, W., "A Feasibility Study of e^N Transition Prediction in Navier–Stokes Methods for Airfoils," *AIAA Journal*, Vol. 37, No. 10, 1999, pp. 1187–1196.

[5] Horton, H. P., and Stock, H. W., "Computation of Compressible, Laminar Boundary Layers on Swept, Tapered Wings," *Journal of Aircraft*, Vol. 32, No. 6, 1995, pp. 1402–1405.

[6] Stock, H. W., and Degenhardt, E., "A Simplified e^N Method for Transition Prediction in Two-Dimensional, Incompressible Boundary Layers," *Zeitung für Flugwissenschaft und Weltraumforschung*, Vol. 13, No. 1, 1989, pp. 16–30.

[7] Warren, E. S., and Hassan, H. A., "Transition Closure Model for Predicting Transition Onset," *Journal of Aircraft*, Vol. 35, No. 5, 1998, pp. 769–775.

[8] Czerwiec, R. M., Edwards, J. R., Rumsey, C. L., Bertelrud, A., and Hassan, H. A., "Study of High-Lift Configurations Using k-ζ Transition/Turbulence Model," *Journal of Aircraft*, Vol. 37, No. 6, 2000, pp. 1008–1016.

[9] Edwards, J. R., Roy, C. J., Blottner, F. G., and Hassan, H. A., "Development of a One-Equation Transition/Turbulence Model," *AIAA Journal*, Vol. 39, No. 9, 2001, pp. 1691–1698.

[10] Kroll, N., Rossow, C. C., Becker, K., and Thiele, F., "The MEGAFLOW Project," Aerospace Science and Technology, Vol. 4, No. 4, 2000, pp. 223–237.

[11] Krumbein, A., and Stock, H. W., "Laminar-Turbulent Transition Modeling in Navier–Stokes Solvers Using Engineering Methods," *ECCOMAS 2000* [CD-ROM], International Center for Numerical Methods in Engineering, Depósito Legal: B-37139-2000, Barcelona, Spain, 2000.

[12] Krumbein, A., "Coupling of the DLR Navier–Stokes Solver FLOWer with an e^N-Database Method for Laminar-Turbulent Transition Prediction on Airfoils," *New Results in Numerical and Experimental Fluid Mechanics III*, Notes on Numerical Fluid Mechanics, Vol. 77, Springer-Verlag, Berlin, 2002, pp. 92–99.

[13] Stock, H. W., and Haase, W., "Navier–Stokes Airfoil Computations with e^N Transition Prediction Including Transitional Flow Regions," *AIAA Journal*, Vol. 38, No. 11, 2000, pp. 2059–2066.

[14] Krumbein, A., "Transitional Flow Modeling and Application to High-Lift Multi-Element Airfoil Configurations," *Journal of Aircraft*, Vol. 40, No. 4, 2003, pp. 786–794.

[15] Stock, H. W., and Krumbein, A., "2D High-Lift RANS Computations with e^N Transition Prediction—A310 Take-Off and Landing Configurations," Deutsches Zentrum für Luft- und Raumfahrt (DLR), Rept. HiAer D1.3-2, Braunschweig, Germany, April 2003.

[16] Stock, H. W., "Navier–Stokes Computations of Laminar Airfoils Using e^N Transition Prediction," Deutsches Zentrum für Luft- und Raumfahrt (DLR), Rept. IB 129-99/18, Braunschweig, Germany, Aug. 1999.

[17] Arthur, M. T., Dol, H., Krumbein, A., Houdeville, R., and Ponsin, J., "Application of Transition Criteria in Navier–Stokes Computations," ONERA, GARTEUR Transition Action Group AD (AG-35), TP137, Toulouse, France, Jan. 2003.

[18] Stock, H. W., "Infinite Swept Wing RANS Computations with e^N Transition Prediction, a Validation Study," Deutsches Zentrum für Luft- und Raumfahrt (DLR), Rept. ALTTA D3.1.2-4, Braunschweig, Germany, Oct. 2002.

[19] Stock, H. W., and Haase, W., "Some Aspects of Linear Stability Calculations in Industrial Applications," *Transitional Boundary Layers in Aeronautics*, edited by R. A. W. M. Henkes and J. L. van Ingen, General Publication Series, AIAA, Reston, VA, 1996, pp. 225–238.

[20] Mack, L. M., "Transition and Laminar Instability," Jet Propulsion Lab., California Inst. of Technology, Publication 77-15, Pasadena, CA, 1977.

[21] "FLOWer—Installation and User Handbook," Institut für Entwurfsaerodynamik, Deutsches Zentrum für Luft- und Raumfahrt e.V., DLR, Release 116, Doc.Nr. MEGAFLOW-1001, Braunschweig, Germany, May 2000.

[22] Dhawan, S., and Narasimha, R., "Some Properties of Boundary Layer Flow During the Transition from Laminar to Turbulent Motion," *Journal of Fluid Mechanics*, Vol. 3, 1958, pp. 418–436.

[23] Walker, G. J., "Transitional Flow on Axial Turbomachine Blading," *AIAA Journal*, Vol. 27, No. 5, 1989, pp. 595–602.

[24] Dargel, G., and Schnieder, H., "GARTEUR AD (AG08) Final Report," MBB Transport- und Verkehrsflugzeuge, GARTEUR High Lift Action Group AD (AG-08), Rept. TP043, Bremen, Germany, Nov. 1989.

[25] Thibert, J. J., "The GARTEUR High Lift Research Programme," *High-Lift System Aerodynamics*, AGARD, Neuilly-sur-Seine, France, 1993, pp. 16-1–16-21.

[26] Brodersen, O., Ronzheimer, A., Ziegler, R., Kunert, T., Wild, J., and Hepperle, M., "Aerodynamic Applications Using MegaCads," *Proceedings of 6th International Conference on Numerical Grid Generation in Computational Field Simulation*, edited by M. Cross, P. Eiseman, J. Häuser, B. K. Soni, and J. F. Thompson, International Society of Grid Generation, National Science Foundation Engineering Research Center for Computational Field Simulation, Mississippi State Univ., Mississippi State, MS, 1998, pp. 793–802.

[27] Manie, F., Piccin, O., and Ray, J. P., "Test Report of the 2D Model M1 in the ONERA F1 Wind Tunnel," GARTEUR High Lift Action Group AD (AG-08), Rept. TP041, ONERA, Chatillon, France, Oct. 1989.

[28] Spalart, P. R., and Allmaras, S. R., "A One-Equation Turbulence Model for Aerodynamic Flows," *La Recherche Aérospatiale*, No. 1, 1994, pp. 5–21.

[29] Edwards, J. R., and Chandra, S., "Comparison of Eddy Viscosity–Transport Turbulence Models for Three-Dimensional, Shock-Separated Flowfields," *AIAA Journal*, Vol. 34, No. 4, 1996, pp. 756–763.

[30] Wilcox, D. C., "Reassessment of the Scale-Determining Equation for Advanced Turbulence Models," *AIAA Journal*, Vol. 26, No. 11, 1988, pp. 1299–1310.

[31] "High Level Modelling of High Lift Aerodynamics-HiAer—Final Technical Report," Swedish Defence Research Agency (FOI), GROWTH Project HiAer, Project No. GRD1-2000-25226, Stockholm, Sweden, April 2004.

[32] Liou, W. W., and Liu, F. J., "Spatial Linear Instability of Confluent Wake/Boundary Layers," *AIAA Journal*, Vol. 39, No. 11, 2001, pp. 2076–2081.

[33] Liu, F. J., Liou, W. W., and Joslin, R. D., "Numerical Simulation of Confluent Wake/Boundary Layer Flows," AIAA Paper 2003-623, Jan. 2003.

[34] de Cock, K. M. J., "2D Maximum Lift Prediction for the 59 Percent Span Wing Section of the A310 Aircraft", National Aerospace Lab. (NLR), Rept. NLR-CR-98500, Amsterdam, The Netherlands, Nov. 1998.

[35] Rudnik, R., Ronzheimer, A., and Schenk, M., "Berechnung von zwei- und Dreidimensionalen Hochauftriebskonfigurationen Durch Lösung der Navier–Stokes Gleichungen," *Jahrbuch 1996-Bd. II der Deutschen Gesellschaft für Luft- und Raumfahrt-Lilienthal-Oberth e.V. (DGLR)—JT 96-104*, Bonn, Germany, 1996, pp. 717–726.